

Lattice Boltzmann simulation of electromechanical resonators in gaseous media

CARLOS E. COLOSQUI¹†, DEVREZ M. KARABACAK²
KAMIL L. EKINCI¹ AND VICTOR YAKHOT¹

¹Department of Mechanical Engineering, Boston University, Boston, MA 02215, USA

²IMEC Holst Centre, Eindhoven, 5605 KN, The Netherlands

(Received 14 April 2009; revised 3 December 2009; accepted 30 December 2009;
first published online 30 March 2010)

In this work, we employ a kinetic-theory-based approach to predict the hydrodynamic forces on electromechanical resonators operating in gaseous media. Using the Boltzmann–BGK equation, we investigate the influence of the resonator geometry on the fluid resistance in the entire range of non-dimensional frequency variation $0 \leq \tau\omega \leq \infty$; here the fluid relaxation time $\tau = \mu/p$ is determined by the gas viscosity μ and pressure p at thermodynamic equilibrium, and ω is the (angular) oscillation frequency. Our results here capture two important aspects of recent experimental measurements that covered a broad range of experimental parameters. First, the experimentally observed transition from viscous to viscoelastic flow in simple gases at $\tau\omega \approx 1$ emerges naturally in the numerical data. Second, the calculated effects of resonator geometry are in agreement with experimental observations.

1. Introduction

Electromechanical resonators with linear dimensions in the nanometre to micrometre scales are being developed for technological applications and fundamental research. One of the most important attributes of these nano/microelectromechanical systems (N/MEMS) resonators is that they have a very small intrinsic dissipation of energy, quantified by their high quality factors $Q_o \sim O(10^2\text{--}10^4)$. N/MEMS resonators are thus ultrasensitive to external perturbations enabling important technologies such as atomic force microscopy (AFM) (Binnig, Quate & Gerber 1982) and biochemical sensing (Ekinci, Huang & Roukes 2004).

Some of the most promising applications of N/MEMS, however, require their immersion in fluid media (e.g. air mixtures or biological fluids), where fluid–device interaction can significantly degrade the overall sensitivity (Sader 1998; Bhiladvala & Wang 2003; Paul & Cross 2004). Numerous efforts are currently underway to overcome this difficulty and develop future N/MEMS for promising nanotechnological and biomedical applications. Unquestionably, the flows generated by N/MEMS demand a novel understanding of fluid mechanics at increasingly smaller time and length scales. Conversely, experimental characterization and numerical analysis of fluid-immersed N/MEMS resonators provide an invaluable opportunity to advance knowledge in new areas of fluid mechanics such as high-frequency nanofluidics. Recent work on high-frequency oscillating flows (Karabacak, Yakhot &

† Present address: Department of Chemical Engineering, Princeton University, Princeton, NJ 08544, USA. Email address for correspondence: colosqui@princeton.edu

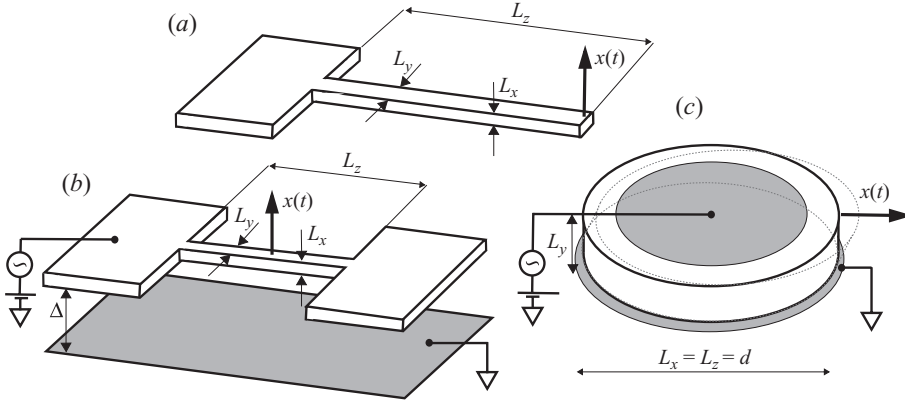


FIGURE 1. (a) Cantilever beam (b) Doubly clamped beam (c) Quartz crystal.

Ekinci 2007; Yakhot & Colosqui 2007; Colosqui *et al.* 2009) reports a viscoelastic transition in simple gases at sufficiently large values of the non-dimensional frequency $\tau\omega$. Here, $\tau = \mu/p$ is the relaxation time in terms of the pressure p and viscosity μ of the gas at equilibrium; ω is the oscillation (angular) frequency; the non-dimensional frequency is also the Weissenberg number for this problem, $Wi = \tau\omega$. Such a remarkable phenomenon is beyond the reach of classical (Newtonian) fluid mechanics, which is only valid for $\tau\omega \ll 1$. The viscoelastic transition is accompanied by a substantial attenuation of the energy dissipated by the fluid and a subsequent improvement in the performance of the fluid-immersed device.

In this study, we solve the Boltzmann–BGK equation (BE–BGK) via numerical procedures based on the rigorous formulation of the lattice Boltzmann–BGK (LBGK) method in Hermite space (Shan, Yuan & Chen 2006; Zhang, Shan & Chen 2006). Previous work demonstrated that consistent LBGK algorithms, using low-order Hermite expansions and so-called regularization procedures, are not constrained to Newtonian hydrodynamics and can effectively model linear viscoelastic behaviour in high-frequency (isothermal) flows (Colosqui *et al.* 2009). The present numerical results show a close agreement with experimental measurements of the energy dissipation on different resonators over a wide range of frequency and pressure variation.

2. Electromechanical resonators

Illustrated in figure 1(a,b) are the first class of studied resonators in the form of cantilever and doubly clamped beams ($L_z \gg L_x \sim L_y$). Harmonic motion in the beams can be induced through the application of periodic electrostatic, photothermal or inertial forces. The beams are driven around their fundamental and first harmonic out-of-plane flexural resonances while optical techniques are used to determine the resonant response (Kouh *et al.* 2005). The doubly clamped beams are suspended above a stationary substrate at a mean height $\Delta \simeq 400$ nm; thus, the presence of the substrate has no significant effect on the fluidic damping (e.g. via squeeze-film damping) (Karabacak *et al.* 2007). We also study a macroscopic quartz crystal resonator (Ekinci, Karabacak & Yakhot 2008). The studied resonator (see figure 1c) is in the form of a thin crystal disk ($L_x = L_z \gg L_y$) connected to electrodes so that its resonances in thickness-shear modes can be electrically excited and detected by

| Class | Dimensions (μm) | $\omega_o/2\pi$ (MHz) | Q_o | S/m_o ($\text{m}^2 \text{kg}^{-1}$) | AR |
|------------------------------|---|--------------------------|-------|--|----|
| Cantilever beam ^a | $L_x = 2.0$ $L_y = 53$ $L_z = 460$ | 0.078 | 8320 | 688 | 26 |
| Cantilever beam ^a | $L_x = 3.6$ $L_y = 36$ $L_z = 125$ | 1.97 | 3520 | 405 | 10 |
| Doubly clamped beam | $L_x = 0.2$ $L_y = 0.23$ $L_z = 9.6$ | 24.2 | 415 | 8380 | 1 |
| Quartz crystal disk | $L_x = L_z = d \simeq 10000$ $L_y \simeq 160$ | 32.7 | 40755 | 6.29 | 0 |

TABLE 1. Electromechanical resonators. ^aFirst harmonic.

piezoelectric effects. In all the measurements, the resonance amplitudes of the beams and crystal resonators are kept extremely small.

Specific dimensions and (vacuum) characteristics, such as the resonance frequency ω_o , quality factor Q_o and surface to modal mass ratio S/m_o , of four studied resonators are listed in table 1. The size of the devices vary from sub-micron to millimetres while their resonance frequencies are in the range of kilohertz to megahertz. Experimental analysis of the four resonators in table 1 is performed with the devices operating in purified nitrogen at room temperature, $T \simeq 300$ K; the pressure is gradually varied from low-vacuum to atmospheric conditions, $0.1 \leq p \leq 1000$ Torr. As the pressure is varied and given that $\tau = \mu/p$, the resulting flows cover a wide range of dimensionless frequency variation $0.001 \leq \tau\omega \leq 10$ (Karabacak *et al.* 2007).

2.1. Resonators immersed in a fluid

The dynamics of an electromechanical resonator immersed in a fluid can be studied by means of a one-dimensional harmonic oscillator approximation (Cleland & Roukes 1998)

$$m_o(x_{tt} + \gamma_o x_t + \omega_o^2 x) = F(t) + F_f(t), \quad (2.1)$$

where m_o is the effective mass corresponding to the vibrational mode (Cleland & Roukes 1998; Karabacak *et al.* 2007), γ_o is the (structural) damping coefficient and ω_o is the resonance frequency of the device in vacuum. The load on the oscillator is produced by the driving force $F(t) = \text{Re}\{F(\omega)e^{-i\omega t}\}$ along with a fluid resistance $F_f(t) = -m_o(\gamma_f x_t + \beta_f x_{tt})$ which has both dissipative and inertial components (Landau & Lifshitz 1959). The oscillation amplitude has the general form $x(t) = \text{Re}\{x(\omega)e^{-i(\omega t + \phi)}\}$ and from (2.1) the frequency response is

$$x(\omega) = \frac{F_0}{m_o} \frac{1}{[\omega_o^2 - \omega^2(1 + \beta_f) - i\omega(\gamma_o + \gamma_f)]}, \quad (2.2)$$

with $F_0 \equiv F(\omega)e^{i\phi}$ being the effective force amplitude. Equation (2.2) includes fluidic effects through the fluidic inertia, or fluid-added mass, β_f and fluidic damping γ_f . Experimental values of the added mass and fluidic dissipation are respectively obtained from the frequency shift and the broadening of the Lorentzian frequency response (2.2) (Karabacak *et al.* 2007). In this study, the fluid-added mass is very small, $\beta_f \ll 1$, and so is the measured shift in the resonance frequency: $\Delta\omega_o/\omega_o \approx \beta_f/2$. The device quality factor in the fluid thus becomes $Q \approx \omega_o/(\gamma_o + \gamma_f)$.

3. Hydrodynamics of high-frequency flows

Similar to previous work (Sader 1998; Bhiladvala & Wang 2003; Paul & Cross 2004), the present analysis is valid when gradients along the spanwise direction of the oscillating body are negligible so that the flow is considered two-dimensional.

This assumption holds for a slender beam ($L_z \gg L_x \sim L_y$) with uniform rectangular cross-section, or a thin disk ($L_x = L_z = d \gg L_y$), where the aspect ratio $AR = L_y/L_x$ (see table 1) becomes the geometric parameter characterizing the dominant chordwise flow. Other dynamically relevant flow parameters are the Mach number $M = U_o/c_s$ and the Reynolds number $Re = \rho U_o L_x/\mu$ determined by the fluid velocity amplitude $U_o = |\omega x(\omega)|$, the speed of sound $c_s \simeq 298 \text{ m s}^{-1}$ and molecular viscosity $\mu \simeq 1.78 \times 10^{-5} \text{ kg m}^{-1} \text{ s}^{-1}$ of nitrogen at room temperature. Given the tiny oscillation amplitude of the resonators, the resulting Mach and Reynolds number are extremely small, $M \sim Re < 0.001$, in all operation conditions. Consequently, the generated flow can be assumed laminar, nearly incompressible and isothermal.

The common approach hitherto encountered in the literature (Sader 1998; Bhiladvala & Wang 2003; Paul & Cross 2004) for the theoretical and/or numerical determination of fluidic effects on resonators is based on the Navier–Stokes (NS) equations for Newtonian fluid flow. However, a fundamental assumption for the applicability of classical NS equations is that hydrodynamic scales are much larger than their kinetic counterparts, i.e. $\tau\omega \ll 1$. Previous work (Karabacak *et al.* 2007; Yakhot & Colosqui 2007; Ekinci *et al.* 2008; Colosqui *et al.* 2009) on high-frequency oscillating flows has established that varying the non-dimensional frequency $\tau\omega$ gives rise to qualitatively different behaviour: purely viscous (Newtonian) for $\tau\omega = 0$, viscoelastic (transitional) for $0 < \tau\omega < \infty$ and purely elastic (free molecular) for $\tau\omega \rightarrow \infty$. While viscous flows are accurately described by Newtonian hydrodynamic equations, an ‘extended’ hydrodynamic description accounting for kinetic (non-equilibrium) phenomena is required at sufficiently large $\tau\omega$ where non-Newtonian behaviour is observed (see Yakhot & Colosqui 2007; Colosqui *et al.* 2009).

3.1. Newtonian hydrodynamics

In the Newtonian regime $\tau\omega \ll 1$, the flow around a body oscillating with very small amplitude $|x(\omega)| \ll L_x$ is governed by the linearized NS equations for incompressible flow (Landau & Lifshitz 1959):

$$\nabla \cdot \mathbf{u} = 0, \quad \frac{\partial \mathbf{u}}{\partial t} = \nu \nabla^2 \mathbf{u} - \frac{1}{\rho} \nabla p. \quad (3.1)$$

After adoption of the standard no-slip boundary conditions, these equations provide well-known analytical solutions for simple geometries (Landau & Lifshitz 1959; Tuck 1969). Through these solutions, one can determine fluidic forces over a body as

$$F_f(t) = \rho B \omega^2 \text{Re}\{\Gamma(\omega)x(\omega)e^{-i(\omega t + \phi)}\},$$

where ρ is the fluid density and B is the body volume; $\Gamma = m_o(\beta_f + i\gamma_f/\omega)/(\rho B)$ is the so-called ‘hydrodynamic’ function. One of the simplest solutions of the unsteady NS equations is obtained for an infinite plate oscillating in a fluid ($L_x = L_z = \infty, L_y = 0$), known as the Stokes’ second problem (Landau & Lifshitz 1959; Yakhot & Colosqui 2007). For a slender body having a thin cross-section with small but finite width ($0 < AR \ll 1$), the Newtonian hydrodynamic function can be approximated by the solution of Stokes’ second problem:

$$\Gamma_{(AR \ll 1)}(\omega) = (1 + i) \frac{S}{B} \sqrt{\frac{\nu}{2\omega}}. \quad (3.2)$$

Here, S is the surface area in contact with the fluid and $\nu = \mu/\rho$. When the cross-section is not small ($AR \gtrsim 1$), the common approach has been to study the flow generated by simpler geometries such as a cylinder with a radius equal to half the

nominal length scale, $r = L_y/2$. For the case of an infinite cylinder with its axis normal to the x -direction, the hydrodynamic function is (Sader 1998; Bhiladvala & Wang 2003; Paul & Cross 2004)

$$\Gamma_{\text{cyl}}(\omega) = 1 + \frac{4i}{\sqrt{i\omega r^2/\nu}} \frac{K_1(-i\sqrt{i\omega r^2/\nu})}{K_0(-i\sqrt{i\omega r^2/\nu})}, \quad (3.3)$$

where K_0 and K_1 are Bessel functions of the third kind. The asymptotic behaviour of the Newtonian hydrodynamic function of a cylinder (3.3) and that of a rectangular beam are similar in both limits $\omega r^2/\nu \rightarrow 0$ and $\omega r^2/\nu \rightarrow \infty$ (Tuck 1969). For this reason, and only within the Newtonian regime ($\tau\omega \ll 1$), the solution for an oscillating cylinder has been employed with some degree of accuracy in estimating fluidic effects on rectangular beams with cross-sections of moderate-to-large aspect ratio (Sader 1998; Bhiladvala & Wang 2003; Paul & Cross 2004). For very large aspect ratios ($L_x \rightarrow 0$), Sader (1998) formulated an empirical correction to (3.3) such that the hydrodynamic function becomes $\Gamma_{(AR \gg 1)} = \Gamma_{\text{cyl}} \Omega(\omega L_y^2/\nu)$. Nevertheless, the correction of Sader (1998) remains essentially unity $|\Omega - 1| = O(10^{-1})$ within all regimes studied in this work.

3.2. Beyond Newtonian hydrodynamics

When flow time scales $\mathcal{T} = 1/\omega$ are of the same order as the relaxation time τ , kinetic effects become significant and Newtonian hydrodynamic equations (3.1) break down. The primary issue encountered beyond Newtonian regimes ($\tau\omega \gtrsim 1$) is the lack of a robust hydrodynamic equation governing the flow. To obtain a hydrodynamic description valid for arbitrary non-dimensional frequencies ($0 \leq \tau\omega \equiv \tau/\mathcal{T} \leq \infty$), one must resort to kinetic theory representations of the flow. Unfortunately, the problem of deriving (closed-form) hydrodynamic equations via kinetic theory, albeit largely studied (see Grad 1949; Cercignani 1969; Chapman & Cowling 1970; Chen, Orszag & Staroselsky 2007), remains essentially open for arbitrary flow regimes.

Another critical point arising when kinetic effects are no longer negligible is that of proper boundary conditions for the hydrodynamic equations at the solid–fluid interface. Hydrodynamic boundary conditions are determined by a rather complex fluid–solid interaction in the vicinity of a solid surface. For flows at finite Knudsen number, the slip boundary condition has been extensively adopted (Park, Bahukudumbi & Beskok 2004; Lauga, Brenner & Stone 2007; Weng 2008). According to Maxwell’s picture of slip of a gas over a solid surface, a finite mean free path $\lambda \sim \tau c_s$ leads to an ‘effective’ slip velocity

$$[\mathbf{u}(\mathbf{x}_w, t) - \mathbf{U}_w] \cdot \mathbf{t} = \frac{2 - \sigma_v}{\sigma_v} \lambda [\nabla(\mathbf{u} \cdot \mathbf{t}) \cdot \mathbf{n} + \nabla(\mathbf{u} \cdot \mathbf{n}) \cdot \mathbf{t}] \quad (3.4)$$

to be employed as boundary condition at the coarse-grained (hydrodynamic) level. Here \mathbf{t} and \mathbf{n} are the unit tangent and normal vectors to a wall located at \mathbf{x}_w and moving with velocity \mathbf{U}_w ; and \mathbf{u} is the fluid velocity. Meanwhile, σ_v is the tangential momentum accommodation coefficient of the solid surface. A unit accommodation coefficient ($\sigma_v = 1$) represents a situation where all fluid particles are diffusively scattered after collision with the wall; the opposite limit ($\sigma_v = 0$) corresponds to the case where all such collisions are specular. First-order Maxwell slip models (3.4) are accurate for steady flow at small to moderate Knudsen numbers ($Kn < 1$) (Park *et al.* 2004; Weng 2008), while high-order versions have been proposed for unsteady shear flow (Park *et al.* 2004; Hadjiconstantinou 2005). The effective slip in oscillating shear flows has recently been investigated via kinetic methods such as LBGK and direct

simulation Monte Carlo (DSMC). Expected functional shapes have been obtained for the slip as a function of the Knudsen number $Kn = \lambda/\mathcal{L}$ in steady shear flows ($\mathcal{L} \sim |\nabla u_t|/|u_t|$) or the non-dimensional frequency $\tau\omega = \tau/\mathcal{T}$ in oscillating shear flows (Park *et al.* 2004; Hadjiconstantinou 2005; Colosqui & Yakhot 2007).

4. Kinetic model of hydrodynamics

At room temperature and under ordinary pressure conditions (ranging from low-vacuum to atmospheric pressure), simple gases are composed of a large number of electrically neutral molecules, each with an effective diameter that is negligible compared to the average intermolecular distance. Under such conditions, the BE–BGK is commonly employed as a kinetic model of the flow (Cercignani 1969; Chen *et al.* 2007). For monatomic gases in the absence of external force fields $\mathbf{F} = 0$, the BE–BGK for the evolution of the Boltzmann distribution $f(\mathbf{x}, \mathbf{v}, t)$ in phase space (\mathbf{x}, \mathbf{v}) reads:

$$\frac{\partial f}{\partial t} + \mathbf{v} \cdot \nabla f = -\frac{f - f^{eq}}{\tau}. \quad (4.1)$$

Without loss of generality, we define $\theta = k_B T/m_{gas} = c_s^2$ and adopt a molecular mass $m_{gas} = 1$; the equilibrium distribution can then be expressed as

$$f^{eq}(\mathbf{x}, \mathbf{v}, t) = \frac{\rho}{(2\pi\theta)^{D/2}} \exp\left[-\frac{(\mathbf{v} - \mathbf{u})^2}{2\theta}\right], \quad (4.2)$$

where D is the velocity space dimension ($\mathbf{v} = v_k \mathbf{e}_k$; $k = 1, D$). Hydrodynamic quantities, like mass density ρ , fluid velocity \mathbf{u} and energy are obtained as moments of the distribution function:

$$\left. \begin{aligned} \int f(\mathbf{x}, \mathbf{v}, t) d\mathbf{v} &= \rho(\mathbf{x}, t), \\ \int f(\mathbf{x}, \mathbf{v}, t) \mathbf{v} d\mathbf{v} &= \rho \mathbf{u}(\mathbf{x}, t), \\ \int f(\mathbf{x}, \mathbf{v}, t) \mathbf{v}^2 d\mathbf{v} &= \rho D \theta(\mathbf{x}, t) + \rho \mathbf{u}^2(\mathbf{x}, t). \end{aligned} \right\} \quad (4.3)$$

Hereafter, since $M = U_o/\sqrt{\theta} \ll 1$ for the studied flow regimes, we assume $\theta \simeq \text{const}$.

The BE–BGK (4.1) must be regarded as an ad hoc or phenomenological model satisfying a few basic symmetries and conservation laws of a real system. Thus, the exact applicability limits of the BE–BGK model will remain questionable until it is rigorously derived from microscopic equations. In the limit of small Knudsen ($Kn \rightarrow 0$) and Weissenberg ($Wi \rightarrow 0$) numbers, the model leads to the NS equations, justifying its approximate validity. In the opposite limits $Kn \gg 1$ and/or $Wi \gg 1$, the accuracy of the BE–BGK model can be tested either by comparison with experimental data or with another, more rigorous, theory. In this paper, interested in oscillating flows in the high-frequency limit $Wi = \tau\omega \gg 1$, we have chosen detailed comparison with experimental data as a criterion to determine the applicability of the employed models in this non-trivial and poorly studied limit.

4.1. Kinetic boundary conditions

For bounded flows, particular solutions of (4.1) will require proper boundary conditions. Within the framework of classical kinetic theory, we consider the gas as bounded by a perfectly elastic and isothermal surface ($\theta_w = \theta$) located at \mathbf{x}_w while

moving with velocity \mathbf{U}_w . Under this depiction, particles impinging on a solid surface with velocity \mathbf{v}' acquire a post-collision velocity \mathbf{v} defined by the scattering kernel $B(\mathbf{v}' \rightarrow \mathbf{v})$. General boundary conditions will then read (Cercignani 1969)

$$|(\mathbf{v} - \mathbf{U}_w) \cdot \mathbf{n}| f(\mathbf{x}_w, \mathbf{v}, t) = \int_{(\mathbf{v}' - \mathbf{U}_w) \cdot \mathbf{n} < 0} |(\mathbf{v}' - \mathbf{U}_w) \cdot \mathbf{n}| B(\mathbf{v}' \rightarrow \mathbf{v}) f(\mathbf{x}_w, \mathbf{v}', t) d\mathbf{v}' \quad (4.4)$$

for $(\mathbf{v} - \mathbf{U}_w) \cdot \mathbf{n} > 0$. In this work, we implement and assess two different kinetic boundary conditions at the fluid–solid interface: diffuse-scattering (DS)

$$f(\mathbf{x}_w, \mathbf{v}, t) = \frac{\rho}{(2\pi\theta)^{D/2}} \exp\left[-\frac{(\mathbf{v} - \mathbf{U}_w)^2}{2\theta}\right]; \quad (\mathbf{v} - \mathbf{U}_w) \cdot \mathbf{n} > 0 \quad (4.5)$$

and bounce-back (BB)

$$f(\mathbf{x}_w, \mathbf{v}, t) = f(\mathbf{x}_w, -\mathbf{v} + 2\mathbf{U}_w, t); \quad (\mathbf{v} - \mathbf{U}_w) \cdot \mathbf{n} > 0, \quad (4.6)$$

where impinging particles [$(\mathbf{v} - \mathbf{U}_w) \cdot \mathbf{n} < 0$] are reflected back with the same relative speed and angle of incidence. While a DS kernel yields hydrodynamic slip in agreement with the Maxwell slip model (3.4) for a fully accommodating surface ($\sigma_v = 1$), the BB model renders no-slip at the wall for all flow regimes (i.e. the surface has negative accommodation coefficient $\sigma_v = -2$). The validity range of each model for the solid–fluid interaction will be assessed by comparing LBGK simulation results using both DS and BB schemes against experimental results.

4.2. Free-molecule hydrodynamics

The non-dimensional frequency $\tau\omega = 2\pi\lambda/\mathcal{L}_{FM}$ is proportional to the ratio of the (equilibrium) mean free path $\lambda = \tau c_s$ to the average distance $\mathcal{L}_{FM} = c_s 2\pi/\omega$ travelled by a particle during one oscillation period. Hence, in the high-frequency limit $\tau\omega \gg 1$ one has $\lambda \gg \mathcal{L}_{FM}$, and free-molecule flow approximations are applicable within a thin ‘ballistic’ layer adjacent to the wall. However, $\mathcal{L}_{FM} \rightarrow 0$ for $\tau\omega \rightarrow \infty$, while fluid particles undergo multiple collisions as they penetrate the heat bath outside the vanishing ‘ballistic’ layer. When the system momentum varies over times smaller than the relaxation time of the heat bath, coupling between microscopic relaxation and hydrodynamic processes can lead to memory effects and other nonlinearities in the transport coefficients (i.a. time-dependent shear viscosity). Due to such strong non-equilibrium phenomena, not modelled by the free-molecule approach described in this section, the fluid system ceases to be Markovian and viscoelastic effects can be observed at macroscopic level.

Employing a free-molecule approximation (Bird, Stewart & Lightfoot 2002), let us analyse an $L_x \times L_y$ rectangular section moving in the x -direction with velocity $\mathbf{u} = u\mathbf{i}$ by assuming that $M = u/\sqrt{\theta} \ll 1$, while the fluid infinitely far away remains at thermodynamic equilibrium and undisturbedly at rest ($\rho_\infty = \rho$, $U_\infty = 0$). In the case of diffusive wall scattering (4.5), the net x -force per unit length is

$$F_f^{DS}(t) = - \left(\sqrt{\frac{8}{\pi}} L_y + \sqrt{\frac{2}{\pi}} L_x \right) \rho \sqrt{\theta} u. \quad (4.7)$$

For the BB model (4.6), which renders no hydrodynamic slip, one has $F_f^{BB} = 2F_f^{DS}$. Similar expressions can be obtained for other models of the gas–surface interaction, e.g. $F_f^{SP}(t) = -(\sqrt{(32)/(\pi)})L_y \rho \sqrt{\theta} u$ for specular reflection models rendering no shear stress. Clearly, under the free-molecule approximation employed, there is no

fluidic inertia ($\beta_f = 0$) and hydrodynamic forces only have a dissipative component ($F_f = f_d u$).

5. Lattice Boltzmann–BGK simulation

The method in this work falls in the class of isothermal LBGK models originally formulated by Shan *et al.* (2006) and investigated by Colosqui *et al.* (2009) for unidirectional flow in non-Newtonian regimes. Discretization of velocity space in a finite number of lattice velocities $\{v_i; i = 1, Q\}$ allows one to reduce the problem of solving (4.1) to that of solving a set of LBGK equations

$$\frac{\partial f_i}{\partial t} + \mathbf{v}_i \cdot \nabla f_i = -\frac{f_i - f_i^{eq}}{\tau}, \quad (5.1)$$

$$f_i^{eq} = w_i \rho \left[1 + \frac{1}{\theta} (\mathbf{v}_i \cdot \mathbf{u}) + \frac{1}{2\theta^2} (\mathbf{v}_i \cdot \mathbf{u})^2 - \frac{1}{2\theta} \mathbf{u}^2 \right] \quad i = 1, Q, \quad (5.2)$$

governing the evolution of each lattice population $f_i(\mathbf{x}, t) = w_i f(\mathbf{x}, \mathbf{v}_i, t)$ in configuration space. The set of LBGK equations (5.1) and (5.2) is formally derived by projecting the continuum BE–BGK equations (4.1) and (4.2) onto the Hilbert space \mathbb{H}^2 spanned by the orthonormal basis of Hermite polynomials up to second order. A Gauss–Hermite quadrature formula determines the lattice velocities \mathbf{v}_i , i.e. integration points, and their associated weights w_i . A quadrature rule with algebraic degree of precision $d \geq 4$ permits the exact numerical integration of the three leading moments (4.3) of the continuum distribution f :

$$\rho(\mathbf{x}, t) = \sum_{i=1}^Q f_i(\mathbf{x}, t), \quad \rho \mathbf{u}(\mathbf{x}, t) = \sum_{i=1}^Q f_i(\mathbf{x}, t) \mathbf{v}_i, \quad \rho(u^2(\mathbf{x}, t) + D\theta) = \sum_{i=1}^Q f_i(\mathbf{x}, t) \mathbf{v}_i^2. \quad (5.3)$$

The particular lattice employed for the present simulations is the D2Q37 (Shan & Chen 2007) (i.e. velocity space dimension $D = 2$, number of lattice velocities $Q = 37$); the weights and velocity abscissae of the lattice are included in Appendix A. After lattice discretization of configuration space ($\Delta \mathbf{x}_i = \mathbf{v}_i \Delta t$), numerical procedures to solve the LBGK equations (5.1) advance in two steps: advection and collision. During the advection step, the streaming of lattice populations $\{f_i; i = 1, Q\}$ is performed along the lattice directions:

$$f_i^{adv}(\mathbf{x}, t) = f_i(\mathbf{x} - \mathbf{v}_i \Delta t, t). \quad (5.4)$$

At the end of the advection step, mass, momentum and energy (5.3) are computed from f_i^{adv} , which allows the explicit evaluation of equilibrium distributions (5.2). Then, the BGK ansatz is applied at the collision step:

$$f_i(\mathbf{x} + \mathbf{v}_i, t + \Delta t) = f_i^{eq} + \left[1 - \frac{\Delta t}{\tau} \right] \widehat{f}_i^{ne}. \quad (5.5)$$

The projected, or ‘dealized’, non-equilibrium component (Zhang *et al.* 2006)

$$\widehat{f}_i^{ne} = \frac{w_i}{2\theta^2} (v_{\alpha i} v_{\beta i} - \theta \delta_{\alpha\beta}) \sum_{j=1}^Q (f_j^{adv} - f_j^{eq}) v_{\alpha j} v_{\beta j}, \quad \alpha, \beta = 1, D \quad i = 1, Q \quad (5.6)$$

ensures that the post-collision distribution f_i is strictly expressed by a linear combination of up to second-order Hermite polynomials, i.e. $f_i \in \mathbb{H}^2$. The projection

procedure (Zhang *et al.* 2006) specified in (5.5) and (5.6) eliminates significant numerical errors due to lattice orientation anisotropy and ‘aliasing’ effects, which are reported for the standard LBGK algorithm in strong non-equilibrium conditions (Zhang *et al.* 2006; Colosqui *et al.* 2009). The hydrodynamic equations rendered by the employed LBGK model have been studied in previous work (Yakhot & Colosqui 2007; Colosqui *et al.* 2009) and are presented in Appendix B.

6. Results

Our approach here is to compare the simulation results to recent experimental measurements. In order to do this, we have used the experimentally available parameters in our simulations and presented our numerical data along with our previous experimental data.

The quantitative analysis of fluidic damping on devices with different sizes and structural features is performed by employing the non-dimensional quantity:

$$\bar{\gamma}_f(\tau\omega, AR) = \frac{\gamma_f}{\rho \sqrt{\frac{\theta}{2}} \frac{S}{m_o}}. \quad (6.1)$$

Here, S/m_o is the ratio of wet area to modal mass reported in table 1. After normalization by the fluid mass density ρ and speed of sound $c_s = \sqrt{\theta}$, the dimensionless damping $\bar{\gamma}_f$ (6.1) is solely determined by the non-dimensional frequency $\tau\omega$ and hydrodynamic shape characterized by the aspect ratio $AR = L_y/L_x$. Based on reported data in table 1, we adopt $AR \simeq 0$ for the quartz resonator and $AR \simeq 1, 10$ and 26 for the beams. Experimentally measured values of the total damping are presented as open symbols in figure 2. These are determined from measurements of the resonant response (2.2) as a function of pressure as discussed above. As observed in figure 2, experimental values of the density-normalized damping $\bar{\gamma}_f$ (6.1) exhibit an increasing dispersion in the upper limit of dimensionless frequency variation $\tau\omega \rightarrow \infty$ where $\gamma_f \rightarrow 0$. This is due to the fact that the measured fluidic effect becomes smaller and smaller as the pressure is lowered and the measured signal is dominated by the finite error $\sim 5\%$ present in all the experimental data. This is discussed in more detail in Karabacak *et al.* (2007).

6.1. Lattice Boltzmann–BGK simulation

Simulations are performed with the D2Q37-H2 model described in §5 and Appendix A. It has been demonstrated (Zhang *et al.* 2006; Colosqui *et al.* 2009) that high-order LBGK models such as D2Q37-H2 with a projection procedure are in exact agreement with extended hydrodynamic descriptions (see Appendix B) previously derived for isothermal and unidirectional flows in both Newtonian and non-Newtonian regimes. In all simulations, $\tau = \mu/p \equiv \nu/\theta$ is readily determined from the gas properties at thermodynamic equilibrium, while the employed Mach number is very low $M = U_o/\sqrt{\theta} \leq 0.01$. Dimensional analyses of the studied oscillating flow (Ekinci *et al.* 2008) indicate that as long as $|x(\omega)| \ll L_x$ and $Re = ML_x/\lambda \lesssim 1$ (i.e. for $L_x/\lambda \lesssim 1/M$), the relevant length scale is not determined by linear geometric dimensions of the body $L_y \sim AR L_x$ but by a dynamic characteristic length δ . This dynamic length emerges as the viscous Stokes layer thickness $\delta = \sqrt{\nu/\omega} = \lambda/\sqrt{\tau\omega}$ for $\tau\omega \ll 1$ and becomes the so-called ‘ballistic’ Stokes layer thickness $\delta = \lambda/\tau\omega$ in the limit $\tau\omega \gg 1$. Dissipative effects are characterized by a length scale $\delta_-(\tau\omega)$ which is of the order of the viscous Stokes layer thickness for $\tau\omega \ll 1$ and becomes of

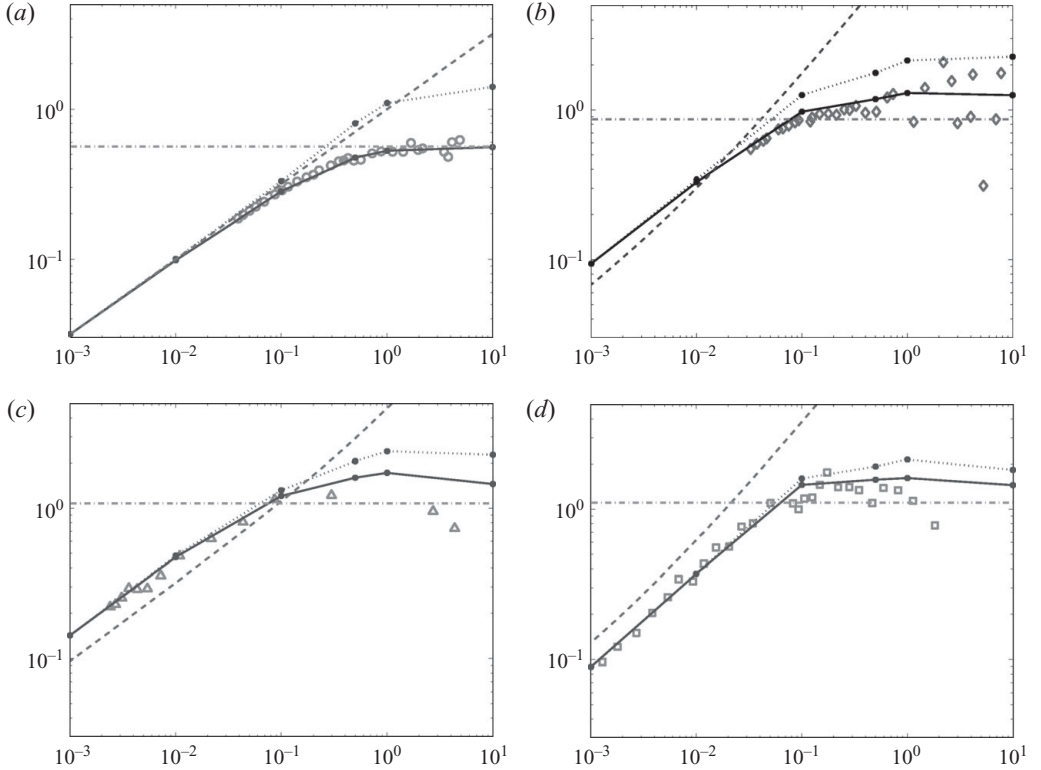


FIGURE 2. Non-dimensional fluid damping $\bar{\gamma}_f(\tau\omega, AR)$ vs. non-dimensional frequency $\tau\omega$. (a) $\omega_o/2\pi = 32.7$ MHz, $AR = 0$. (b) $\omega_o/2\pi = 24.2$ MHz, $AR = 1$. (c) $\omega_o/2\pi = 1.97$ MHz, $AR = 10$. (d) $\omega_o/2\pi = 0.078$ MHz, $AR = 26$. Open symbols represent experimental data. In the LBGK simulations two boundary conditions are used. The solid lines (and closed circles) are the result from D2Q37-H2 with DS at $\tau\omega = 0.001, 0.01, 0.1, 0.5, 1$ and 10 . Similarly, the dotted lines (and closed circles) correspond to D2Q37-H2 with BB. The dashed lines are calculated using the Newtonian fluid approximation. The dashed-dotted lines are the free-molecular (DS) results.

the order of the mean free path as $\tau\omega \rightarrow \infty$. Grid convergence tests corroborate such previous dimensional analyses: while geometric dimensions of the oscillating section were varied in a wide range ($0.01 \lesssim L_x/\lambda \lesssim 100$), simulation results showed no significant variation for spatial resolution $\Delta x \leq \delta/30$ (i.e. $\Delta t \omega \leq 1/30$).

The simulation domain is a periodic box of approximate size $\sim 20\text{--}40L_x \times 20\delta_-$ with an oscillating rectangular section ($L_x \times L_y$) in the centre; a Cartesian grid with uniform resolution is employed in all cases. For the employed numerical setup, the damping of ‘longitudinal’ modes imposed a hard constraint on the minimum length of the computational domain; this constraint becomes especially critical to the computational cost in the high-frequency regimes as $\tau\omega \rightarrow \infty$. Simulation results on different resonators obtained by the D2Q37-H2 model for $\tau\omega = 0.001, 0.01, 0.1, 0.5, 1$ and 10 are compared against experimental data and available analytical expressions for Newtonian and free-molecular flows in figure 2.

The employed LBGK models yield quantitative agreement with experimental measurements over a wide range of non-dimensional frequency $0.001 \leq \tau\omega \leq 10$ for different device geometries and dimensions (table 1). On the other hand, Newtonian fluid approximations such as (3.2) for the quartz disk ($AR \simeq 0$) and (3.3) for the beams

($AR \geq 1$) (Sader 1998; Bhiladvala & Wang 2003; Paul & Cross 2004) give acceptable agreement only within the low-frequency limit $\tau\omega < 0.1$. It is important to note that all Newtonian predictions largely overestimate the fluidic dissipation in the frequency range $\tau\omega > 0.1$. In the high-frequency limit $\tau\omega \gg 1$, only kinetic approaches such as LBGK simulation and the free-molecular flow solution given by (4.7) are in good agreement with the experiment.

6.2. Fluid–solid interaction and boundary schemes

Owing to the small amplitude of oscillation ($|x(\omega)| \ll L_x$), the solid boundary can be assumed to remain static. Only the boundary velocity $\mathbf{U}_w = U_o \sin(\omega t)\mathbf{i}$ varies in time with velocity amplitude $U_o < \omega\Delta x$ such that the displacement amplitude is smaller than the distance between neighbouring lattice nodes. Two boundary schemes are employed in LBGK simulation when modelling the moving walls: the DS and BB schemes described in §4 (see Appendix A for implementation details). While a properly implemented BB scheme (Zou & He 1997) renders no-slip as hydrodynamic boundary condition, the DS model produces an effective slip velocity between the body surface and the fluid immediately adjacent to it. Experimental results in figure 2 show that numerical schemes rendering no-slip at the wall overpredict the fluidic dissipation when $\tau\omega \geq 0.1$. On the other hand, the DS scheme which models the resonator surface as fully accommodating ($\sigma_v = 1$) yields a close agreement with the experimental data in the entire studied range $0.001 \leq \tau\omega \leq 10$.

6.3. Quality factor and fluidic effects

Since fluidic inertia is very small ($\beta_f \ll 1$) for the studied flow conditions, the quality factor of the fluid-immersed device is

$$Q = Q_o \frac{1}{1 + \rho\sqrt{\frac{\theta}{2}} \frac{S}{m_o\gamma_o} \bar{\gamma}_f(\tau\omega, AR)}. \quad (6.2)$$

Evidently, dissipative effects quantified by the structural dissipation $\gamma_o = \omega_o/Q_o$ and fluidic damping $\gamma_f = \rho\sqrt{\theta/2} (S)/(m_o)\bar{\gamma}_f$ determine the device performance. The quality factors reported for the four studied devices are compared against numerical predictions in figure 3. We observe that LBGK simulation (model D2Q37-H2 with DS wall treatment) is in close agreement with experimental data obtained for different cross-sections ($0 \leq AR \leq 26$) in a wide range of operation conditions ($0.1 \leq p \leq 1000$ Torr, $0.078 \leq \omega_o \leq 24$ MHz).

7. Conclusions

Experimental measurements of fluidic effects on dissimilar electromechanical resonators have been compared against available analytical approaches, i.e. the Newtonian flow and free-molecular flow approximations, as well as against kinetic-based simulations presented in §5. Clearly, Newtonian and free-molecular flow models fail to describe transitional flow in the region $0.1 \leq \tau\omega \leq 10$. On the other hand, LBGK simulation accounting for specific geometrical features accurately represents the fluidic damping γ_f in the studied regimes: viscous or Newtonian ($\tau\omega \leq 0.1$), viscoelastic ($0.1 \leq \tau\omega \leq 10$) and elastic ($\tau\omega \geq 10$).

7.1. Viscoelastic dynamics in high-frequency flows

An interesting outcome of our work is the quantitative description of an experimentally observed viscoelastic transition at $\tau\omega \approx 1$. In kinetic theory, the

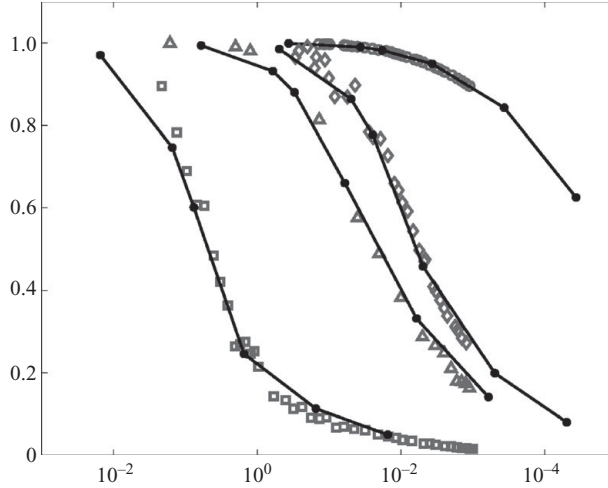


FIGURE 3. Normalized quality factor $Q/Q_o = (\gamma_o)/(\gamma_o + \gamma_f)$ vs. pressure p (Torr). Open symbols represent experimental data as above: (\circ) $\omega_o/2\pi = 32.7$ MHz, $AR = 0$; (\diamond) $\omega_o/2\pi = 24.2$ MHz, $AR = 1$; (\triangle) $\omega_o/2\pi = 1.97$ MHz, $AR = 10$; (\square) $\omega_o/2\pi = 0.078$ MHz, $AR = 26$. Closed dots and the solid lines are the results of LBGK simulations (D2Q37-H2 with DS) at $\tau\omega = 0.001, 0.01, 0.1, 0.5, 1$ and 10 .

breakdown of the NS equations at $Kn = O(1)$ and/or $Wi = O(1)$ is usually attributed to ballistic dynamics or kinetic effects associated with the relatively low frequency of inter-particle collisions. Kinetic equations predict that inertial forces become dominant in the high-frequency limit ($Wi = \tau\omega \rightarrow \infty$), while viscous terms vanish in the hydrodynamic limit. The ‘viscoelastic’ response observed here at sufficiently large Weissenberg number ($Wi = \tau\omega \gg 1$) is linked to the underlying microscopic dynamics, i.e. kinetic and ‘viscoelastic’ effects correspond to the same phenomenon in the studied systems.

The invalidity of Newtonian approaches as $\tau\omega \rightarrow \infty$ is not only due to surface effects, which might be absorbed by proper hydrodynamic boundary conditions, but also due to the qualitatively different fluid dynamics in the bulk. LBGK simulation closely reproduces the experimentally observed (figure 2) saturation of density-normalized dissipation ($\bar{\gamma}_f \rightarrow \text{const}$) in the high-frequency limit $\tau\omega \rightarrow \infty$. This remarkable phenomenon involves a gradual transition from viscous to viscoelastic to purely elastic flow of a simple gas that has been reported by previous theoretical (Yakhot & Colosqui 2007; Colosqui *et al.* 2009) and experimental (Karabacak *et al.* 2007) studies. The viscoelastic response of simple gases in the high-frequency limit is a well-known phenomenon within the realm of transport theory and statistical physics (Evans & Morriss 2008); diffusion processes in non-equilibrium systems can only be established after a finite time $\mathcal{T}_D \sim \tau$ of the order of the relaxation time. In the short-time limit $t < \tau$, where diffusion effects are still weak and transport coefficients such as shear viscosity become frequency dependent (Evans & Morriss 2008), one observes an ensuing decay in the dissipation of fluid momentum and energy.

7.2. Near-wall phenomena

Kinetic effects are significant within the so-called Knudsen layer, e.g. at distances from the solid boundary that are smaller than one mean free path. Kinetic parameters, such as the relaxation time and mean free path, are not easily determined in the near-wall region where the gas–surface interaction plays a critical role. Even when

$\tau\omega \ll 1$, Newtonian fluid models for the stress break down within a mean free path from the wall and NS equations can only be applied outside the Knudsen layer. The concept of having effective slip as proper boundary condition for the hydrodynamic (coarse-grained) equations must be understood within this context. Our kinetic model of the flow based on the BE–BGK is rather simple and does not accurately represent the Knudsen layer; it relies on a single constant relaxation time $\tau = \mu/p$ and kinetic boundary conditions (4.4) determined by surface scattering kernels $B(\mathbf{v}' \rightarrow \mathbf{v})$ for a perfectly elastic and isothermal surface. Nevertheless, the kinetic model in this work accurately predicts hydrodynamic effects such as fluid resistance and mean energy dissipation via adoption of a Maxwell scattering kernel with surface accommodation $\sigma_v = 1$ (i.e. the DS scheme explained in §4). The net effect of the studied gas–surface interactions can be assessed by comparing results in figure 2 for DS (slip) and BB (no-slip) schemes in the range $0.001 \leq \tau\omega \leq 10$ for different cross-sections $0 \leq AR \leq 26$. The reduction in fluid damping solely due to effective slip is found in the interval 0–0.4.

7.3. Resonator performance beyond the Newtonian regime

The decay of the energy dissipated by the fluid as $\tau\omega \rightarrow \infty$ has beneficial effects on the resonator performance. Under relevant experimental conditions, fluidic damping largely dominates over structural dissipation, $\gamma_f \gg \gamma_o$, and thus, $Q \approx \omega/\gamma_f$. In such conditions, the quality factor will actually increase linearly with the operation frequency, $Q \propto \omega$ for $\tau\omega > 1$, instead of the square-root dependence, $Q \propto \sqrt{\omega}$, observed for Newtonian flow $\tau\omega \ll 1$. Therefore, it is advantageous to operate the resonator at a frequency $\tau\omega > 1$ well within the viscoelastic regime. This could be accomplished either by increasing the resonance frequency or by decreasing the effective relaxation time of the fluid through less trivial mechanisms, e.g. through polymer addition or foams for water. Other strategies that can potentially improve the device performance include modifying the cross-sectional shape and surface properties. As observed in figure 2 for the entire range $0.001 \leq \tau\omega \leq 10$, bodies with small aspect ratios, $AR = L_y/L_x \ll 1$, generate less fluidic damping at the same operation frequency and surrounding gas conditions. On the other hand, the employment of super-hydrophobic coatings for resonators in water can further increase the effective hydrodynamic slip with a subsequent reduction of the resistance forces.

7.4. Lattice Boltzmann–BGK simulation of high-frequency flows

LBGK simulations are in close agreement with both analytical predictions and experimental data over a wide range of pressure $0.1 \leq p \leq 1000$ Torr and frequency variation $0.001 \leq \tau\omega \leq 10$. While some rigorous equations of motion may be superior to the ad hoc BE–BGK model, we believe that our work demonstrates the ability of the method to capture non-trivial features of high-frequency flows. This situation is not unique; there exist many examples of successful applications of semi-qualitative models to complicated physical problems.

The authors acknowledge Dr Hudong Chen and Dr Xiaowen Shan from EXA corporation for their support in the development of the employed numerical tools. This work was funded by the National Science Foundation (NSF) under grant CBET-0755927.

Appendix A. The LBGK model D2Q37

Velocity abscissae and weights of the D2Q37 lattice model (Shan *et al.* 2006; Shan & Chen 2007) are presented in table 2.

| v_i/c^a | States | w_i |
|-----------|--------|----------------------|
| (0, 0) | 1 | 0.233150669132352000 |
| (1, 0) | 4 | 0.107306091542219000 |
| (±1, ±1) | 4 | 0.057667859888794800 |
| (2, 0) | 4 | 0.014208216158450700 |
| (±2, ±2) | 4 | 0.001011937592673570 |
| (3, 0) | 4 | 0.000245301027757717 |
| (±1, ±2) | 8 | 0.005353049000513770 |
| (±1, ±3) | 8 | 0.000283414252994198 |

TABLE 2. Model parameters D2Q37. ^aLattice constant: $c = 1.19697977039307 \sqrt{\theta}$.

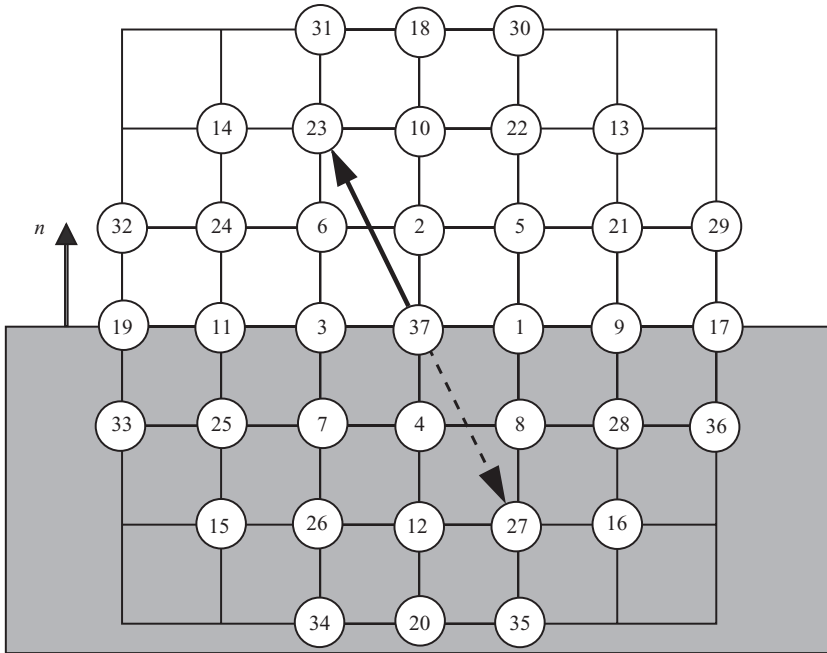


FIGURE 4. D2Q37 lattice cell: solid boundary.

A.1. Boundary conditions

As determined by velocity abscissae in table 2, the D2Q37 lattice cell spans three adjacent nodes in each direction (see figure 4). Realization of boundary conditions requires prescribing the distribution function of, at least, three nodes within the boundary interior. Note that geometric features of size smaller than a lattice cell, e.g. sharp corners, can not be resolved and are therefore smoothed out. Boundary schemes can be readily implemented for simple geometries, such as the ones studied here, having constant surface-normal direction $\mathbf{n} = n_1 \mathbf{i} + n_2 \mathbf{j}$ with either $n_1 = 0$ or $n_2 = 0$. As shown in figure 4, the opted scheme places the solid boundary, moving at velocity \mathbf{u}_{wall} , at the cell centre. A local equilibrium distribution $f_i = f_i^{eq}(\rho, \mathbf{u}_{wall}, \theta)$ is prescribed for nodes at the boundary and interior nodes lying along the negative normal direction ($-\mathbf{n}$). The DS boundary treatment is implemented with no further steps while the BB scheme is realized by ‘reflecting back’ the non-equilibrium components $f_i^{ne} = f_i - f_i^{eq}$

| | | |
|-----------------------------|-----------------------------|-----------------------------|
| $f_2^{ne} = f_4^{ne}$ | $f_{14}^{ne} = f_{16}^{ne}$ | $f_{24}^{ne} = f_{28}^{ne}$ |
| $f_5^{ne} = f_7^{ne}$ | $f_{18}^{ne} = f_{20}^{ne}$ | $f_{29}^{ne} = f_{33}^{ne}$ |
| $f_6^{ne} = f_8^{ne}$ | $f_{21}^{ne} = f_{25}^{ne}$ | $f_{30}^{ne} = f_{34}^{ne}$ |
| $f_{10}^{ne} = f_{12}^{ne}$ | $f_{22}^{ne} = f_{26}^{ne}$ | $f_{31}^{ne} = f_{35}^{ne}$ |
| $f_{13}^{ne} = f_{15}^{ne}$ | $f_{23}^{ne} = f_{27}^{ne}$ | $f_{32}^{ne} = f_{36}^{ne}$ |

TABLE 3. Bounce-back rule D2Q37.

according to the usual rule described in table 3. The standard advection step (5.4) can be thus applied to all nodes outside the boundary.

Appendix B. Hydrodynamic approximation in \mathbb{H}^2

The lattice Boltzmann method can be rigorously formulated within the framework of Galerkin methods (Shan *et al.* 2006). A second-order LBGK model thus derived seeks a solution in the function space \mathbb{H}^2 spanned by Hermite polynomials of order ≤ 2 ($f_i \in \mathbb{H}^2$). The advection step in the LBGK (5.4) algorithm is not consistent with standard Galerkin procedures where Galerkin coefficients are computed while the approximate solution remains within a finite function space. Hence, the projection of the post-advection distribution (see (5.6)) is critical for consistency with Galerkin approximations. The formal approximation in \mathbb{H}^2 is given by the following Hermite expansions:

$$f^{eq}(\mathbf{x}, \mathbf{v}, t) = f^M(\mathbf{v}) \left[M_{eq}^{(0)} + \frac{1}{\theta} \mathbf{M}_{eq}^{(1)} : \mathbf{v} + \frac{1}{2\theta^2} (\mathbf{M}_{eq}^{(2)} - M_{eq}^{(0)}\theta\mathbf{I}) : (\mathbf{v}\mathbf{v} - \theta\mathbf{I}) \right], \quad (B 1)$$

and

$$f(\mathbf{x}, \mathbf{v}, t) = f^M(\mathbf{v}) \left[M^{(0)} + \frac{1}{\theta} \mathbf{M}^{(1)} : \mathbf{v} + \frac{1}{2\theta^2} (\mathbf{M}^{(2)} - M^{(0)}\theta\mathbf{I}) : (\mathbf{v}\mathbf{v} - \theta\mathbf{I}) \right], \quad (B 2)$$

where $f^M = \exp(-\mathbf{v}^2)/(2\pi\theta)^{D/2}$ and $I_{\alpha\beta} = \delta_{\alpha\beta}$. The relations above involve the n -order velocity moments

$$\mathbf{M}^{(n)}(\mathbf{x}, t) = \int f(\mathbf{x}, \mathbf{v}, t) \mathbf{v}^n d\mathbf{v} \quad (B 3)$$

and their equilibrium counterparts $\mathbf{M}_{eq}^{(n)} = \int f^{eq} \mathbf{v}^n d\mathbf{v}$, which are explicit functions of low-order moments ($n \leq 2$) related to conserved quantities;

$$\mathbf{M}^{(0)} = \mathbf{M}_{eq}^{(0)} = \rho, \quad \mathbf{M}^{(1)} = \mathbf{M}_{eq}^{(1)} = \rho\mathbf{u}, \quad \text{trace}(\mathbf{M}^{(2)}) = \text{trace}(\mathbf{M}_{eq}^{(2)}) = \rho(u^2 + D\theta). \quad (B 4)$$

The zero- and first-order moment equations (i.e. mass and momentum equations) from BE–BGK are

$$\left(1 + \tau \frac{\partial}{\partial t} \right) \mathbf{M}^{(0)} + \tau \nabla \cdot \mathbf{M}^{(1)} = \mathbf{M}_{eq}^{(0)} \quad (B 5)$$

and

$$\left(1 + \tau \frac{\partial}{\partial t} \right) \mathbf{M}^{(1)} + \tau \nabla \cdot \mathbf{M}^{(2)} = \mathbf{M}_{eq}^{(1)}. \quad (B 6)$$

As usual, to define a closed system of governing equations for the studied isothermal system, we need to express high-order moments entering (B 6) in terms of the conserved

quantities (B4). Multiply (B6) by $(1 + \tau \partial_t)$ and rearrange to get

$$\left(1 + \tau \frac{\partial}{\partial t}\right)^2 \mathbf{M}^{(1)} = \left(1 + \tau \frac{\partial}{\partial t}\right) [\mathbf{M}_{eq}^{(1)} - \tau \nabla \cdot \mathbf{M}^{(2)}], \quad (\text{B } 7)$$

then take divergence of the moment equation for the second order

$$\left(1 + \tau \frac{\partial}{\partial t}\right) \nabla \cdot \mathbf{M}^{(2)} = \nabla \cdot [\mathbf{M}_{eq}^{(2)} - \tau \nabla \cdot \mathbf{M}^{(3)}]. \quad (\text{B } 8)$$

Using (B8) in (B7) gives

$$\left(1 + \tau \frac{\partial}{\partial t}\right)^2 \mathbf{M}^{(1)} = \left(1 + \tau \frac{\partial}{\partial t}\right) \mathbf{M}_{eq}^{(1)} - \tau \nabla \cdot \mathbf{M}_{eq}^{(2)} + \tau^2 \nabla \cdot \nabla \cdot \mathbf{M}^{(3)}. \quad (\text{B } 9)$$

We now compute the third-order moment above using (B2) for $f_i \in \mathbb{H}^2$:

$$\mathbf{M}_{\alpha\beta\gamma}^{(3)}(\mathbf{x}, t) = \rho\theta(u_\alpha \delta_{\beta\gamma} + u_\beta \delta_{\alpha\gamma} + u_\gamma \delta_{\alpha\beta}). \quad (\text{B } 10)$$

Recalling that $\mathbf{M}^{(1)} = \mathbf{M}_{eq}^{(1)} = \rho\mathbf{u}$ (B4), $\mathbf{M}_{eq}^{(2)} = \rho(\mathbf{u}\mathbf{u} + \theta\mathbf{I})$, and plugging (B10) into (B9) leads to

$$\left(1 + \tau \frac{\partial}{\partial t}\right) \frac{\partial}{\partial t} \rho\mathbf{u} + \nabla \cdot (\rho\mathbf{u}\mathbf{u}) = -\nabla \rho\theta + \tau \nabla \cdot [\nabla(\rho\theta\mathbf{u}) + \nabla^T(\rho\theta\mathbf{u}) + \nabla \cdot (\rho\theta\mathbf{u}\mathbf{I})]. \quad (\text{B } 11)$$

In the case of nearly incompressible and isothermal flow ($M \ll 1$), (B11) approximates the NS equations for Newtonian fluids as $\tau\omega \rightarrow 0$; this conclusion is a well-known result for second-order LBGK models. For $\tau\omega \geq 0$, the same arguments employed in §3.1 allow for the linearization of the momentum (B11) in the classical small-amplitude limit $M\sqrt{\theta}/\omega \ll L_x$. For low-Mach number flow over small-amplitude oscillating bodies, the hydrodynamic equations (B7) and (B8) then become

$$\frac{\partial}{\partial t} \rho + \nabla \cdot \rho\mathbf{u} = 0, \quad (\text{B } 12)$$

$$\left(\tau \frac{\partial^2}{\partial t^2} + \frac{\partial}{\partial t}\right) \rho\mathbf{u} = \mu \nabla^2 \mathbf{u} - \nabla p, \quad (\text{B } 13)$$

after adopting $\mu = \rho\tau\theta$ and $p = \rho\theta$. Notice that expansions about equilibrium were not employed in the derivation of (B12) and (B13). Within the framework of Hermite space approximation $f \in \mathbb{H}^2$, we obtain a closed-form hydrodynamic description based on the BE–BGK that is, in principle, not constrained to Newtonian regimes. Provided that the Gauss–Hermite quadrature associated with the lattice has algebraic degree of precision $d \geq 4$ and projection in \mathbb{H}^2 is enforced, the approximate LBGK solution will converge to the exact solution of (B12) and (B13) as time–space resolution increases (Colosqui *et al.* 2009).

The wave-diffusion equation (B13), which becomes the telegrapher’s equation in the case of unidirectional shear flow ($\nabla p = 0$), has already been successfully employed to analytically predict the fluidic dissipation in small-amplitude oscillating flows over a wide range of non-dimensional frequency $\tau\omega$ (Karabacak *et al.* 2007; Ekinici *et al.* 2008).

REFERENCES

- BHILADVALA, R. B. & WANG, Z. J. 2003 Effect of fluids on the Q factor and resonance frequency of oscillating micrometre and nanometre scale beams. *Phys. Rev. E* **69**, 036307.

- BINNIG, G., QUATE, C. F. & GERBER, C. 1982 Atomic force microscope. *Phys. Rev. Lett.* **56**, 930.
- BIRD, R. B., STEWART, W. E. & LIGHTFOOT, E. N. 2002 *Transport Phenomena*. Wiley & Sons.
- CERCIGNANI, C. 1969 *Mathematical Methods in Kinetic Theory*. Plenum.
- CHAPMAN, S. & COWLING, T. G. 1970 *The Mathematical Theory of Non-Uniform Gases*. Cambridge University Press.
- CHEN, H., ORSZAG, S. A. & STAROSELSKY, I. 2007 Macroscopic description of arbitrary Knudsen number flow using Boltzmann–BGK kinetic theory. *J. Fluid Mech.* **574**, 495–505.
- CLELAND, A. N. & ROUKES, M. L. 1998 A nanometre-scale mechanical electrometer. *Nature* **392**, 161.
- COLOSQUI, C. E., CHEN, H., SHAN, X., STAROSELSKY, I. & YAKHOT, V. 2009 Propagating high-frequency shear waves in simple fluids. *Phys. Fluids* **21**, 013105.
- COLOSQUI, C. E. & YAKHOT, V. 2007 Lattice Boltzmann simulation of a non-Newtonian oscillating flow in a high-frequency limit. *Intl J. Mod. Phys. C* **18** (4), 473–482.
- EKINCI, K. L., HUANG, X. M. & ROUKES, M. L. 2004 Ultrasensitive nanoelectromechanical mass detection. *Appl. Phys. Lett.* **84**, 4469.
- EKINCI, K. L., KARABACAK, D. M. & YAKHOT, V. 2008 Universality in Oscillating Flows. *Phys. Rev. Lett.* **101**, 26.
- EVANS, D. & MORRIS, G. 2008 *Statistical Mechanics of Nonequilibrium Liquids*. Cambridge University Press.
- GRAD, H. 1949 On the kinetic theory of rarefied gases. *Commun. Pure Appl. Math.* **2** (4), 331–407.
- HADJICONSTANTINO, N. G. 2005 Oscillatory shear-driven gas flows in the transition and free-molecular-flow regimes. *Phys. Fluids* **17**, 100611.
- KARABACAK, D. M., YAKHOT, V. & EKINCI, K. L. 2007 High-frequency nanofluidics: an experimental study using nanomechanical resonators. *Phys. Rev. Lett.* **98**, 254505.
- KOUH, T., KARABACAK, D., KIM, D. H. & EKINCI, K. L. 2005 Diffraction effects in optical interferometric displacement detection in nanoelectromechanical systems. *Appl. Phys. Lett.* **86**, 013106.
- LANDAU, L. D. & LIFSHITZ, E. M. 1959 *Fluid Mechanics*. Pergamon.
- LAUGA, E., BRENNER, M. P. & STONE, H. A. 2007 Microfluidics: the no-slip boundary condition. In *Handbook of Experimental Fluid Mechanics* (ed. J. Foss, C. Tropea & A. Yarin), Chap. 19, pp. 1219–1240. Springer.
- PARK, J. H., BAHUKUDUMBI, P. & BESKOK, A. 2004 Rarefaction effects on shear driven oscillatory gas flows: a direct simulation Monte Carlo study in the entire Knudsen regime. *Phys. Fluids* **16**, 317.
- PAUL, M. R. & CROSS, M. C. 2004 Stochastic dynamics of nanoscale mechanical oscillators immersed in a viscous fluid. *Phys. Rev. Lett.* **92** (23), 235501–235501.
- SADER, J. E. 1998 Frequency response of cantilever beams immersed in viscous fluids with applications to the atomic force microscope. *J. Appl. Phys.* **84**, 64.
- SHAN, X. & CHEN, H. 2007 A general Multiple-Relaxation Boltzmann Collision Model. *Intl J. Mod. Phys. C* **18** (04), 635–643.
- SHAN, X., YUAN, X. F. & CHEN, H. 2006 Kinetic theory representation of hydrodynamics: a way beyond the Navier–Stokes equation. *J. Fluid Mech.* **550**, 413–441.
- TUCK, E. O. 1969 Calculation of unsteady flows due to small motions of cylinders in a viscous fluid. *J. Engng Math.* **3** (1), 29–44.
- WENG, H. C. 2008 A challenge in Navier–Stokes-based continuum modelling: Maxwell–Burnett slip law. *Phys. Fluids* **20**, 106101.
- YAKHOT, V. & COLOSQUI, C. E. 2007 Stokes’ second flow problem in a high-frequency limit: application to nanomechanical resonators. *J. Fluid Mech.* **586**, 249–258.
- ZHANG, R., SHAN, X. & CHEN, H. 2006 Efficient kinetic method for fluid simulation beyond the Navier–Stokes equation. *Phys. Rev. E* **74** (4), 046703.
- ZOU, Q. & HE, X. 1997 On pressure and velocity boundary conditions for the lattice Boltzmann BGK model. *Phys. Fluids* **9** (6), 1591–1598.